Constraints on magma storage conditions based on geodetic volume change and erupted magma volume and application to the 2011 and 2018 eruptions at Kirishima Shinmoe-dake volcano, Japan

Tomofumi Kozono[1]*, Takehiro Koyaguchi[2], Hideki Ueda[1], Taku Ozawa[1] and Tadashi Yamasaki[3]

Abstract We investigated magma storage conditions prior to the 2011 and 2018 eruptions at Kirishima Shinmoe-dake volcano in Japan based on the relationship between geodetic volume change of magma chamber and erupted magma volume. We derived an analytical expression for the ratio of the erupted magma volume to the geodetic volume change ("volume ratio"), which was formulated as a function of parameters related to the magma storage conditions. This expression shows that the volume ratio is strongly dependent on the effective compressibility of the magma chamber, which in turn depends on the rigidity of surrounding host rocks and shape of the chamber. For the Shinmoe-dake eruptions, the magnitude of the volume change (i.e., deflation) of a spherical magma chamber associated with lava effusion was estimated based on geodetic observations. The erupted magma volume was estimated from a SAR image analysis of the lava accumulation inside the summit crater. Based on these observations, we estimated that the volume ratio in 2011 and 2018 was 2.69 and 2.33, respectively. Substituting the estimated volume ratio into the analytical expression revealed that the observed geodetic data and volume ratio can be explained only when the magma chamber, which was assumed to be spherical, is filled with bubble-free magma. This result suggests that efficient gas segregation from the chamber occurred prior to the eruptions. Our results indicate that combining multi-observation data based on the volume ratio provides valuable information about the magma storage process, such as the behavior of the gas phase in the magma chamber.

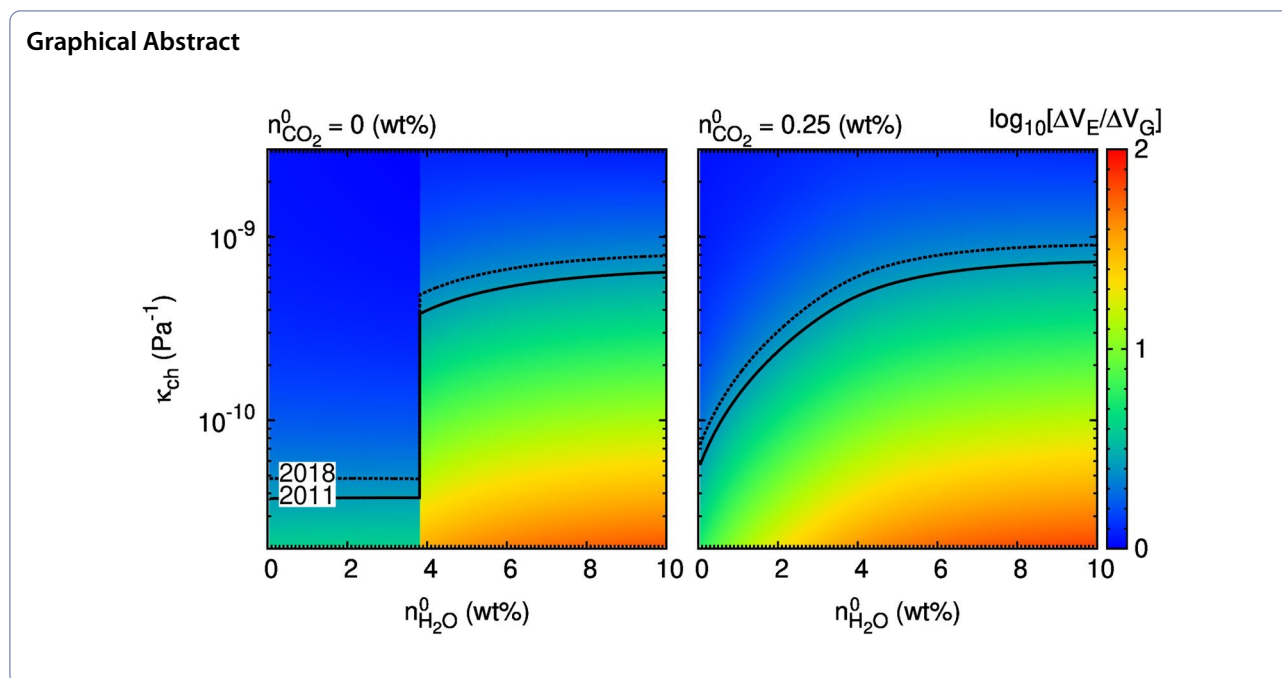**Keywords** Volcanic eruption, Magma chamber, Magma dynamics, Geodetic observation

*Correspondence:
Tomofumi Kozono
kozono@bosai.go.jp
Full list of author information is available at the end of the article

Kozono *et al. Earth, Planets and Space*   (2023) 75:100

Page 2 of 15

Graphical Abstract

Introduction

The magma storage process in a magma chamber is one of the fundamental factors controlling the dynamics of volcanic eruptions (e.g., Tait et al. 1989; Woods and Huppert 2003). Inflation or deflation of the magma chamber in response to magma injection or ejection is a principal process that reflects the status of volcanic activity. Furthermore, storage conditions at the magma chamber correspond to the boundary conditions of the magma ascent flow in the volcanic conduit (conduit flow). The conduit flow is a crucial process controlling eruption styles, with competition between vesiculation and gas escape determining whether the eruption style is explosive or effusive (e.g., Woods and Koyaguchi 1994; Slezin 2003; Kozono and Koyaguchi 2009). Since conduit flow features are sensitive to the boundary conditions, the magma storage process also affects eruption styles through the conduit flow dynamics. Recent progress in multi-observation techniques of volcanic eruptions enables us to obtain detailed constraints on the magma storage process in the magma chamber. For example, thermodynamic conditions in the magma chamber are constrained by petrological observations (e.g., Devine et al. 1998; Suzuki et al. 2013; Tomiya et al. 2013), the size and shape of the magma chamber are inferred based on seismic velocity and resistivity structure anomalies obtained from seismic and magnetotelluric observations (e.g., Lees 2007; Waite and Moran 2009; Hill et al. 2009; Aizawa et al. 2014), and the position and volume change of the magma chamber are estimated from geodetic observations (e.g., Dvorak and Dzurisin 1997; Dzurisin 2003; Segall 2010). In addition, geological and remote sensing surveys of lava flow and dome and eruption cloud at the surface allow us to quantitatively determine the magma discharge rate during eruptions. Combining these observation provides useful information about the relationship between magma chamber dynamics and eruption styles (e.g., Hreinsdóttir et al. 2014; Kozono et al. 2014; Anderson and Poland 2016) and improves our understanding of the magma storage process in the magma chamber.

Determining both the erupted magma volume and geodetic volume change of the magma chamber has the potential to provide valuable information about the magma storage process. When a magma chamber that is embedded into an elastic half-space deflates under the ejection of compressible magma, the ratio of the erupted magma volume to the geodetic volume change of the magma chamber (referred to as "the volume ratio") is described as a function of the compressibility of magma in the magma chamber and effective compressibility of the magma chamber (e.g., Mastin et al. 2008; Segall 2010; Kozono et al. 2013). These compressibilities depend on magma properties, including the composition and vesicularity, and the geometry of the storage. Therefore, we can estimate the magma storage conditions from multi-observations of the geodetic volume change and erupted magma volume.

Kirishima Shinmoe-dake volcano in southern Kyushu, Japan, is densely monitored by multi-observation techniques including geodetic, seismic, geological, geochemical, petrological, and remote sensing measurement devices. The recent activity of this volcano is characterized by the two eruptions in 2011 and 2018 (Nakada et al. 2013; Yamada et al. 2019). Both events presented lava effusion in the summit crater, Vulcanian explosions, and ash emissions, although the former eruption started with three sub-Plinian eruptions, which were not observed in the latter. Continuous tilt measurements throughout the period from 2010 to the present by the National Research Institute for Earth Science and Disaster Resilience (NIED) enabled us to capture the crustal deformation associated with the deflation of the source (e.g., magma chamber) caused by magma effusion to the surface (Ueda et al. 2013; Ueda 2018). Based on these measurements, we can estimate the geodetically required volume change at each lava effusion event. Furthermore, SAR satellite imaging of the lava accumulated inside or outside the summit crater (Ozawa and Kozono 2013; NIED 2018) made it possible to estimate the erupted lava volume. These simultaneous measurements provide an excellent opportunity to estimate the volume ratio during the two eruptions.

In this study, we discuss the magma storage conditions prior to the 2011 and 2018 eruptions at Shinmoe-dake volcano in terms of the geodetic volume change of the magma chamber and the erupted magma volume. The analysis based on the volume ratio has already been applied to the 2011 Shinmoe-dake eruption in a previous study by Kozono et al. (2013). However, these authors mainly focused on estimating the magma discharge rate, and did not in depth investigate the magma storage conditions because of the limited petrological and geochemical information available at that time. At present, progress in petrological and geochemical analyses (e.g., Saito et al. 2023; Suzuki et al. 2013; Tomiya et al. 2013) enables us to obtain detailed information about the storage conditions based on a precise description of the volume ratio as a function of the magmatic and geological parameters. In this study, we firstly refer to observations of the geodetic volume change and erupted volume measured by tiltmeters and SAR satellite imaging, respectively. Second, we present an analytical expression for the volume ratio as a function of the magma storage conditions. Third, we estimate the volume ratio for the Shinmoe-dake eruptions based on the observation data. Finally, we specify the magma storage conditions by substituting the estimated volume ratio into the analytical expression. The present analysis enables us to determine a possible range of effective compressibilities

of the magma chamber, which are used to provide strong constraints on the magma storage process, such as the behavior of the gas phase in the chamber.

The 2011 and 2018 Shinmoe-dake eruptions: observations and data

Shinmoe-dake volcano is an active andesitic stratovolcano located in southern Kyushu, Japan, and it forms part of the Kirishima volcano group (Fig. 1). The following brief descriptions of the 2011 and 2018 eruptions are mainly based on Japan Meteorological Agency (JMA) reports. The main phase of the 2011 eruptions began on January 26 (Japan Standard Time (UTC+9) are used hereafter), and it was characterized by sub-Plinian eruptions and subsequent lava effusion. On January 26 PM, 27 AM, and 27 PM, three major sub-Plinian eruptions were detected by weather radar eruption cloud echo measurements (Shimbori et al. 2013). A small lava dome was formed inside the summit crater in the morning of January 28. This dome changed to a pancake-shaped lava mass that grew continuously between January 29 and 31. In addition to these main events, several infrasound-generating Vulcanian explosions were reported. The 2018 eruptions began on March 1, and ash emissions lasted until March 9. Effusion of new lava inside the summit crater continued between March 6 and 9, and the lava started to effuse outside the crater on March 9. Thirty-four Vulcanian explosions also occurred on March 6 and
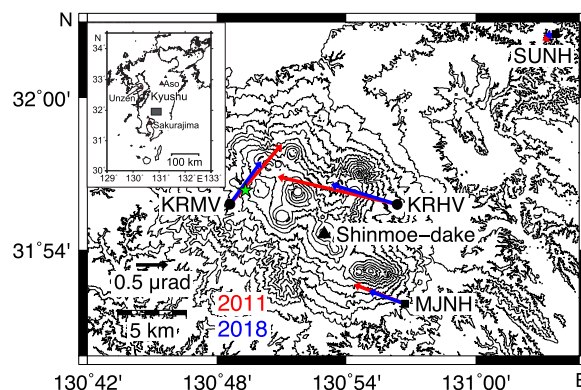

Fig. 1 Topographic map of the Kirishima volcano group in Kyushu Island, Japan, with the location of Shinmoe-dake volcano (shown by a triangle) and the locations of the tilt stations of V-net (circles; KRHV and KRMV) and Hi-net (squares; SUKH and MJNH) networks by NIED. Observed crustal deformations during the 2011 (red) and 2018 (blue) eruptions are shown as tilt-down vectors, and an asterisk indicates the surface projection of a spherical deformation source of the 2011 eruption at a depth of 9.8 km BSL determined from tiltmeter and GPS data crustal deformation measurements (Ueda et al. 2013; Ueda 2018). Maps were constructed using Wessel et al. (2013) and 10-m digital mesh maps provided by Geospatial Information Authority of Japan

7. After March 9, several Vulcanian explosions and slow lava flow (flow distance is about 150 m) were observed.

During the 2011 and 2018 eruptions, borehole-type tiltmeters of the volcano observation network (V-net; 200-m deep) and high-sensitivity seismograph network (Hi-net; 100-m deep) stations operated by NIED measured crustal deformation, which implied deflation of a magma chamber beneath the center of the Kirishima volcano group (Fig. 1; Ueda et al. 2013; Ueda 2018). The direction of the tilt vectors in each station was almost the same between 2011 and 2018, suggesting that the position and shape of the source magma chamber were unchanged during these eruptions while the magnitude of the tilt change was larger in 2011 than 2018 (Fig. 1). A source model for the 2011 eruption that best fits the tilt and GNSS data selected through a generic algorithm and Akaike's information criterion (AIC) was one with a single spherical source (magma chamber) that was 6.5 km to the northwest of the summit of Shinmoe-dake at a depth of 9.8 km below sea level (Fig. 1). A preliminary analysis of the 2018 eruption, in which a spherical source was assumed because of the same tilt direction between 2011 and 2018 (Fig. 1), showed that the source was located at $\sim$ 7 km to the northwest of the summit at a depth of 9.6 km (Ueda 2018). This implies a generally consistent deflation source between 2011 and 2018. The total magnitudes of the geodetic volume change in the deflation source (ΔV_G) during the eruptions in 2011 and 2018 were estimated as 1.32×10^7 m^3 and 6.9×10^6 m^3, respectively (Fig. 2a, b; Ueda et al. 2013; Ueda 2018). The difference in the total magnitude of ΔV_G between 2011 and 2018 is explained by the fact that the deflation in 2011 was accompanied by the sub-Plinian eruptions and the lava effusion while that in 2018 was caused only by the lava effusion (Kozono et al. 2013; Yamada et al. 2019). Nakao et al. (2013) also evaluated the location and the volume change of the spherical deflation source during the 2011 eruption using GNSS data from 14 stations. The estimated horizontal position of the deflation source was almost the same as that estimated by Ueda et al. (2013), and the source depth and the geodetic volume change were estimated as 8.35 km and 1.335×10^7 m^3, respectively.

The topography and the volume of erupted lava (ΔV_E) in 2011 and 2018 were estimated based on day-by-day SAR analyses of lava accumulation inside the summit crater (Fig. 2c, d; Ozawa and Kozono 2013; NIED 2018) In the analyses, the contributions of the topography to backscatter intensity in the PALSAR and TerraSAR-X images (in 2011), and PALSAR-2 and COSMO-SkyMed images (in 2018) are simulated using a digital terrain map and a GAMMA SAR processor,
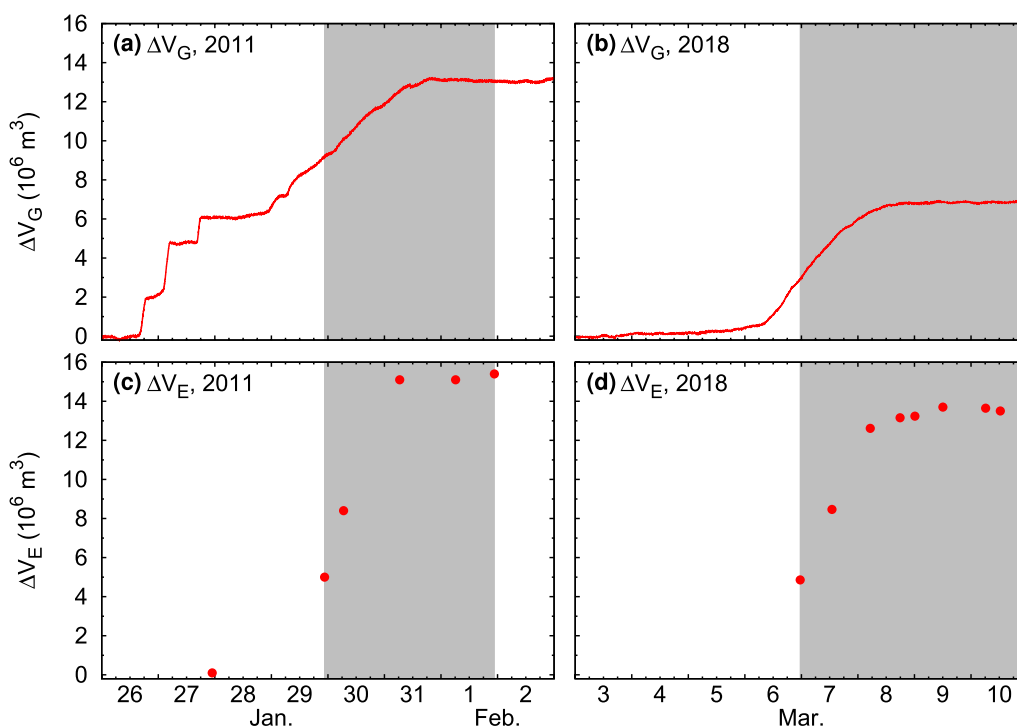
Fig. 2 Magnitude of the geodetic volume change in the deflation source (ΔV_G; **a, b**) and erupted lava volume (ΔV_E; **c, d**) as a function of time during the 2011 (**a, c**) and 2018 (**b, d**) eruptions of Kirishima Shinmoe-dake volcano (Ueda et al. 2013; Ueda 2018; Ozawa and Kozono 2013; NIED 2018). Time windows used for calculating ΔV_E/ΔV_E are shown by shaded ranges

Kozono *et al. Earth, Planets and Space*   (2023) 75:100

Page 5 of 15

and the SAR images are connected with the geographical coordinates by matching it with the simulated images. The maximum values of $\Delta V_{\rm E}$ in 2011 and 2018 were estimated to be 1.54×10^7 m^3 and 1.40×10^7 m^3, respectively (Fig. 2c, d; Ozawa and Kozono 2013; NIED 2018). Here $\Delta V_{\rm E}$ is related to the erupted mass (ΔM) as $\Delta M = \rho_{\rm e} \Delta V_{\rm E}$, where $\rho_{\rm e}$ is the density of the erupted lava. Generally, $\rho_{\rm e}$ becomes lower than the density of non-vesiculated magma ($\sim 2,500$ kg m^{-3}) because of pore structures in the lava.

A petrological study of the 2011 Shinmoe-dake eruptions shows a complex magma plumbing system from the 10 km depth magma chamber to the surface, including two magma chambers at 10 and 5 km depths (i.e., a dual-magma-chamber system; Suzuki et al. 2013). The deeper magma chamber is composed of basaltic andesite magma, and the ascent of this magma to the shallower chamber causes mixing with silicic andesite magma. Then, the mixed magma ascended to the surface, leading to eruptions. Such dual-magma-chamber system has, however, a concern that the petrological imaging of the chamber system is not always consistent with the geodetic imaging (Kozono 2021). The geodetic observations of the Shimoe-dake eruptions also showed that the petrologically inferred shallower source was not detected (Nakao et al. 2013; Ueda et al. 2013). In this study, we focus only on the deeper chamber (i.e., 8.35 or 9.8 km below sea level), the one having been inferred from both the petrological and geodetic studies, where its storage conditions are to be constrained. The missing shallower chamber in the geodetic study requires a more detailed analysis, e.g., the contrast of the magma compressibility between the deeper and shallower chambers in the dual-chamber system (Kozono 2021). This, however, is beyond the scope of this study, leaving it as a matter to investigate further in a future study.

Thorough estimates of $\Delta V_{\rm G}$ and $\Delta V_{\rm E}$ have been performed for the 2011 eruption (Ueda et al. 2013; Ozawa and Kozono 2013), whereas only preliminary results have been obtained for the 2018 eruption (Ueda 2018; NIED 2018). Petrological analyses of the magma storage conditions are also limited to the 2011 eruption (e.g., Suzuki et al. 2013; Tomiya et al. 2013), because detailed petrological information is not available for the 2018 eruption. Therefore, the main target of our study should be the 2011 eruption. $\Delta V_{\rm G}$ and $\Delta V_{\rm E}$ in 2011 and 2018 were estimated using the same method under the same accuracy, indicating that data for the 2018 eruption are also valuable for investigating the magma storage conditions. In addition, similarities were observed in the deformation pattern (Fig. 1) and the lava effusion process (Fig. 2c, d) between the

two eruptions, implying a common magma plumbing system. In this study, we also use $\Delta V_{\rm G}$ and $\Delta V_{\rm E}$ data for the 2018 eruption to analyze the magma storage conditions.

Analytical expression for $\Delta V_{\rm E}/\Delta V_{\rm G}$

In this section, we derive an analytical expression for the ratio of the erupted volume to the geodetic volume change (i.e., the volume ratio; $\Delta V_{\rm E}/\Delta V_{\rm G}$) as a function of the magma properties and geological conditions. Although the expression for $\Delta V_{\rm E}/\Delta V_{\rm G}$ has already been provided in previous studies (e.g., Mastin et al. 2008; Rivalta and Segall 2008; Segall 2010; Kozono et al. 2013), we show the expression as explicitly as possible so that it can be used in future studies in other eruption cases.

When an elastically deformable magma chamber filled with compressible magma deflates in response to magma ejection from the chamber to the surface, the volume ratio is expressed from the mass conservation of the magma as (e.g., Mastin et al. 2008; Segall 2010; Kozono et al. 2013):

$$\frac{\Delta V_{\rm E}}{\Delta V_{\rm G}} = \frac{\rho_{\rm m}}{\rho_{\rm e}}\left(\frac{\kappa_{\rm m}}{\kappa_{\rm ch}} + 1\right), \tag{1}$$

where $\rho_{\rm m}$ is the magma density in the magma chamber, $\rho_{\rm e}$ is again the density of the erupted lava, and $\kappa_{\rm m}$ is the magma compressibility in the magma chamber, defined as follows:

$$\kappa_{\rm m} \equiv \frac{1}{\rho_{\rm m}}\frac{d\rho_{\rm m}}{dp}. \tag{2}$$

Here, $\kappa_{\rm ch}$ is the effective compressibility that connects the volume change of the chamber caused by elastic deformation of the surrounding host rocks with the pressure change of the magma chamber (referred to as the "effective chamber compressibility"). Under the assumption of no relative velocity between the gas and liquid in the magma chamber (i.e., closed system), $\rho_{\rm m}$ is expressed as follows:

$$\rho_{\rm m} = \left(\frac{nRT}{p} + \frac{1-n}{\rho_{\rm lc}}\right)^{-1}, \tag{3}$$

where n is the mass fraction of gas in the magma chamber, p is the pressure, R is the gas constant, T is the temperature, and $\rho_{\rm lc}$ is the density of liquid-crystals mixture in the magma chamber:

$$\rho_{\rm lc} = (1-\beta)\rho_{\rm l} + \beta\rho_{\rm c}, \tag{4}$$

where β is the crystal volume fraction in the chamber (i.e., phenocryst content) and $\rho_{\rm l}$ and $\rho_{\rm c}$ are the densities

of the liquid and crystal, respectively. The dependence of ρ_l on temperature, pressure, and melt compositions was modeled based on Lange and Carmichael (1990) and Iacovino and Till (2019). Under the assumption of equilibrium volatile exsolution, n is expressed as follows:

$$n = \frac{n_0 - n_l c}{1 - n_l c} \, (n > 0),\tag{5}$$

where n_0 is the initial volatile content, c is the dissolved volatile concentration, and n_l is the mass fraction of liquid with respect to liquid + crystals:

$$n_l = \frac{(1-\beta)\rho_l}{\rho_{lc}}.\tag{6}$$

We assume that the volatile is composed of H_2O and CO_2, and its concentration is controlled by the solubility model of Iacono-Marziano et al. (2012) (Fig. 3). In this case, n_0 and c are expressed as $n_{H_2O}^0 + n_{CO_2}^0$ and $c_{H_2O} + c_{CO_2}$, respectively, where the subscripts denote the volatile species. From Eqs. (1), (2), and (3), we obtain the analytical expression for $\Delta V_E / \Delta V_G$ as a function of the magmatic and the geological parameters:

$$\frac{\Delta V_E}{\Delta V_G} = \frac{\rho_m}{\rho_e}\left[\frac{\rho_m}{\kappa_{ch}}\left\{\frac{(1-n)\kappa_{lc}}{\rho_{lc}} + \frac{nRT}{p^2} - \frac{nT}{p}\frac{dR}{dp} + \left(\frac{1}{\rho_{lc}} - \frac{RT}{p}\right)\frac{dn}{dp}\right\} + 1\right],\tag{7}$$

where κ_{lc} is the compressibility of the liquid-crystal mixture expressed from Eq. (4) as follows:

$$\kappa_{lc} \equiv \frac{1}{\rho_{lc}}\frac{d\rho_{lc}}{dp} = \frac{(1-\beta)\rho_l}{\rho_{lc}}\kappa_l + \frac{\beta\rho_c}{\rho_{lc}}\kappa_c.\tag{8}$$

Here, κ_l and κ_c are the compressibilities of the liquid and the crystal, respectively. The explicit forms of ρ_l, ρ_c, κ_l, κ_c, n, R, dn/dp, and dR/dp are shown in the Appendix. In the
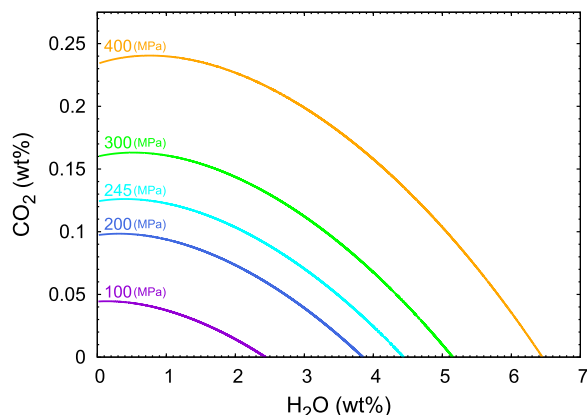
Fig. 3 Solubility of H_2O–CO_2 mixture obtained by Iacono-Marziano et al. (2012) for $T = 1303$ K and melt compositions of the Shinmoe-dake eruptions (Suzuki et al. 2013), with varying pressure

case of no volatile exsolution, $n = 0$ so that $\Delta V_E / \Delta V_G$ is rewritten as

$$\left.\frac{\Delta V_E}{\Delta V_G}\right|_{n=0} = \frac{\rho_{lc}}{\rho_e}\left(\frac{\kappa_{lc}}{\kappa_{ch}} + 1\right).\tag{9}$$

Results

Volume ratio estimation

We estimated the volume ratio ($\Delta V_E / \Delta V_G$) during the Shinmoe-dake eruptions using the observations of ΔV_G and ΔV_E (Fig. 2). To calculate the volume ratio, we selected a time window in which both ΔV_G and ΔV_E were precisely estimated (shaded ranges in Fig. 2). We defined the time window as a range between the time at which a confidential estimation of the lava volume started and the time at which the lava volume reached the maximum. This time window corresponds to the later period of the lava effusion phase. In the selected time windows, the values of $\Delta V_E / \Delta V_G$ were estimated as 2.69 and 2.33 in 2011 and 2018, respectively. In this study we do not use ΔV_E for the sub-Plinian phase of the 2011 eruption (cf. Kozono et al. 2013) to avoid unnecessary uncertainties associated with volume estimations. The estimated values are summarized in Table 1.

Specifying the magma storage conditions

Constraints on the magma storage conditions in the magma chamber are inferred from the estimated values of $\Delta V_E / \Delta V_G$ based on Eqs. (7) and (9). Since our analysis focuses on the deeper magma chamber at ~ 10 km depth, we set the magmatic parameters based on the information about the basaltic andesite magma reported by Suzuki et al. (2013): the estimated temperature and the crystallinity were 1303 K and 8.9 vol.%, respectively, and the melt compositions were inferred from the average

Table 1 Magnitude of the geodetic volume change in the deflation source (ΔV_G), erupted magma volume (ΔV_E), and $\Delta V_E / \Delta V_G$ in the later period of lava effusion during the 2011 and 2018 Shinmoe-dake eruptions (shown by shaded ranges in Fig. 2)

Year	Period	ΔV_G (10^6 m^3)	ΔV_E (10^6 m^3)	$\Delta V_E / \Delta V_G$
2011	22:36, Jan. 29–22:39, Feb. 1	3.87	10.40	2.69
2018	23:30, Mar. 6–23:16, Mar. 10	3.92	9.13	2.33

Kozono *et al. Earth, Planets and Space*   (2023) 75:100

Page 7 of 15

compositions of the melt inclusions (Table 1 of Suzuki et al. 2013). When these quantities are fixed, $\Delta V_E / \Delta V_G$ in Eqs. (7) and (9) depends on the initial volatile contents ($n_{H_2O}^0$ and $n_{CO_2}^0$), effective chamber compressibility, pressure, and density of the erupted magma. We first summarize how $\Delta V_E / \Delta V_G$ depends on these parameters below.
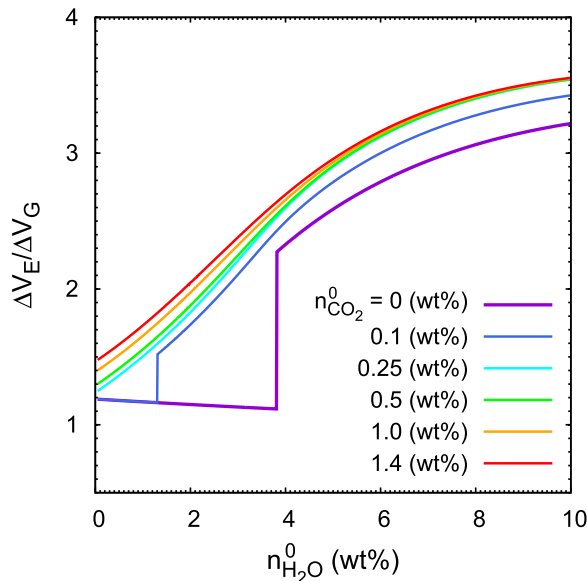

Fig. 4 $\Delta V_E / \Delta V_G$ as a function of initial H_2O content ($n_{H_2O}^0$) with varying initial CO_2 content ($n_{CO_2}^0$) obtained from Eq. (7) or (9). The compressibility of the magma chamber (κ_{ch}), pressure (p), and density of the erupted magma (ρ_e) are set to 5×10^{-10} Pa^{-1}, 245 MPa, and 2500 kg m^{-3}, respectively

Figures 4 and 5 show the dependence of $\Delta V_E / \Delta V_G$ and magma compressibility (κ_m) on $n_{H_2O}^0$ and $n_{CO_2}^0$ based on Eqs. (2), (7), and (9). In Fig. 5, we also show the compressibilities of the liquid (κ_l), crystals (κ_c), and liquid+crystals (κ_{lc}), which indicated that κ_l and κ_{lc} are ~ 6–7×10^{-11} Pa^{-1}, and κ_c is $\sim 10^{-11}$ Pa^{-1}. The relationship between $\Delta V_E / \Delta V_G$ and $n_{H_2O}^0$ is characterized by two regions in the lower- and higher-$n_{H_2O}^0$ ranges in which $\Delta V_E / \Delta V_G$ slightly decreases with increasing $n_{H_2O}^0$ in the lower-$n_{H_2O}^0$ range but drastically increases with $n_{H_2O}^0$ in the higher-$n_{H_2O}^0$ range (Fig. 4). This contrasting feature originates from the dependence of κ_m on the volatile contents (Fig. 5; Huppert and Woods 2002). In the lower-$n_{H_2O}^0$ range, volatiles are not exsolved because n_0 is less than $n_l c$; therefore, $n = 0$ (see Eq. (5)) and κ_m is equal to the compressibility of the liquid-crystal mixture κ_{lc} (Fig. 5a). In this case, $\Delta V_E / \Delta V_G$ is expressed by Eq. (9). Since the density of H_2O is lower than those of other oxide components, the liquid density decreases with increasing $n_{H_2O}^0$, thus leading to a slight decrease in $\Delta V_E / \Delta V_G$ in this range (Fig. 4). In the higher-$n_{H_2O}^0$ range, volatile exsolution occurs under the condition of $n > 0$, in which the existence of the gas phase causes an abrupt increase in κ_m (Fig. 5a) and $\Delta V_E / \Delta V_G$ (cf. Equation 7). In this range, the liquid density is independent of $n_{H_2O}^0$ because the liquid phase is saturated with volatiles. The gas phase increases with $n_{H_2O}^0$ following Eq. (5), thus leading to an increase in κ_m (Fig. 5) and $\Delta V_E / \Delta V_G$ (Fig. 4). The increase in κ_m or $\Delta V_E / \Delta V_G$ with $n_{CO_2}^0$ for a given $n_{H_2O}^0$ (Figs. 4, 5) is also caused by the increase in the gas phase. Because the H_2O–CO_2 solubility (Fig. 3)
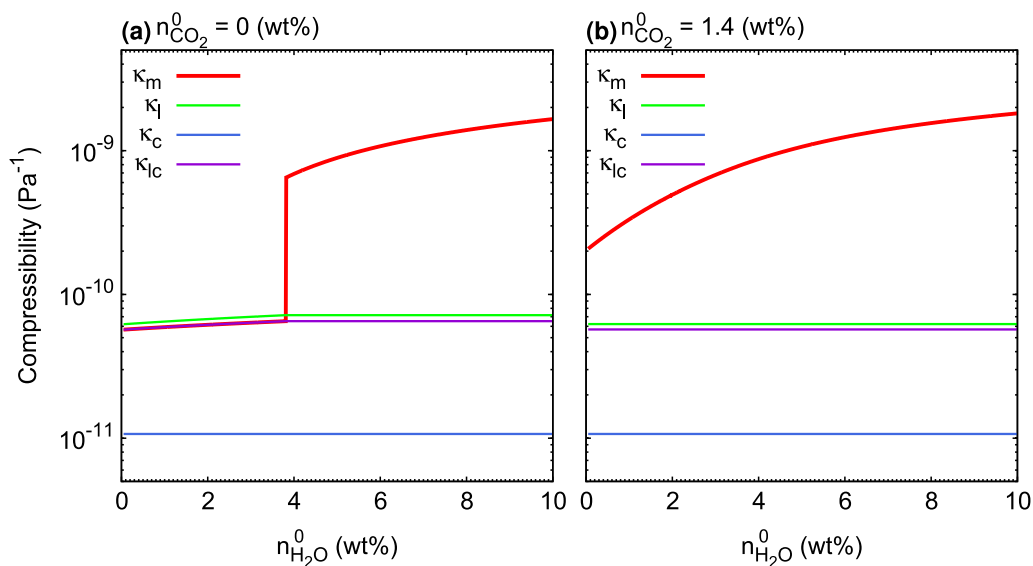
Fig. 5 Compressibilities of magma (κ_m), liquid (κ_l), crystals (κ_c), and liquid + crystals (κ_{lc}) as a function of the initial H_2O content ($n_{H_2O}^0$) and varying initial CO_2 contents ($n_{CO_2}^0$). Results for (**a**) $n_{CO_2}^0 = 0$ wt%; and (**b**) $n_{CO_2}^0 = 1.4$ wt%. The pressure (p) is set as 245 MPa

Kozono *et al. Earth, Planets and Space*   (2023) 75:100

Page 8 of 15
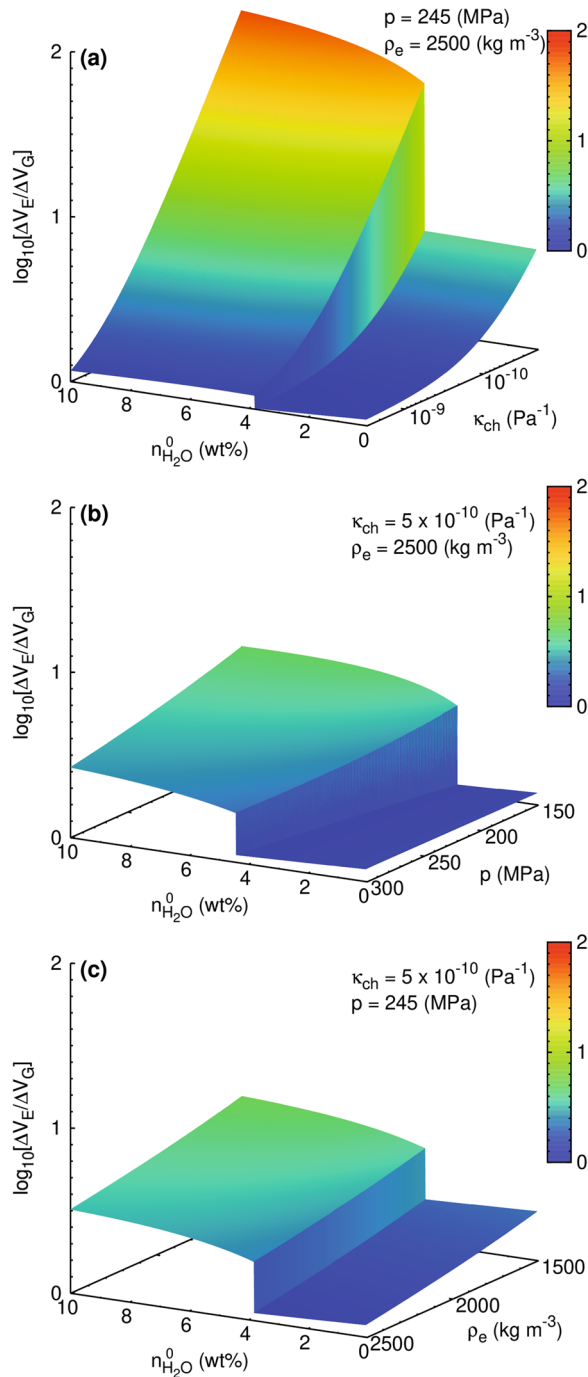
Fig. 6 Dependence of the relationship between $\Delta V_E / \Delta V_G$ and $n_{H_2O}^0$ on κ_{ch}, p, and ρ_e for $n_{CO_2}^0 = 0$ wt%, obtained from Eq. (7) or (9). Results for (**a**) 2×10^{-11}–3×10^{-9} Pa^{-1}, $p = 245$ MPa, and $\rho_e = 2500$ kg m^{-3}; (**b**) $\kappa_{ch} = 5 \times 10^{-10}$ Pa^{-1}, $p = 150$–300 MPa, and $\rho_e = 2500$ kg m^{-3}; and (**c**) $\kappa_{ch} = 5 \times 10^{-10}$ Pa^{-1}, $p = 245$ MPa, and $\rho_e = 1500$–2500 kg m^{-3}

shows that the critical value of $n_{H_2O}^0$ for the volatile exsolution decreases with increasing $n_{CO_2}^0$, the range of $n_{H_2O}^0$ for $n > 0$ increases with $n_{CO_2}^0$ (Fig. 4; Mastin et al. 2008).

$\Delta V_E / \Delta V_G$ also depends on the effective compressibility of the magma chamber (κ_{ch}) as well as the pressure (p) and the density of the erupted magma (ρ_e) (Fig. 6). By maintaining the contrasting feature of $\Delta V_E / \Delta V_G$ in the lower and higher $n_{H_2O}^0$ ranges, $\Delta V_E / \Delta V_G$ increases with decreasing κ_{ch} (Fig. 6a), p (Fig. 6b), and ρ_e (Fig. 6c). The increase in $\Delta V_E / \Delta V_G$ with decreasing p is caused by the increase in magma compressibility due to the efficient volatile exsolution and vesiculation as well as the increase in the gas compressibility. In Fig. 6a, the range of the effective chamber compressibility (2×10^{-11} -3×10^{-9} Pa^{-1}) was set based on the plausible rigidity range of the surrounding host rocks (3–30 GPa) and chamber shape with an aspect ratio up to 10 (see the "Discussion" for details). In Fig. 6b, the pressure range was set as 150–300 MPa under the assumption that the overpressure at the magma chamber is ±30 MPa with respect to the lithostatic pressure by considering the strength of the surrounding host rocks (e.g., Rubin 1995). Here the lithostatic pressure was calculated to be 180–270 MPa on the basis of the geodetically estimated chamber depth: 7.36–10.84 km considering 95% confidence intervals (Nakao et al. 2013; Ueda et al. 2013). In Fig. 6c, the range of ρ_e (1500–2500 kg m^{-3}) corresponds to the case in which the porosity of the erupted magma is 0–40 vol.%. Under these changes in p and ρ_e, the variation in $\Delta V_E / \Delta V_G$ for fixed initial volatile contents is less than one order of magnitude. In contrast, the variation in $\Delta V_E / \Delta V_G$ with κ_{ch} is more drastic, especially at the higher-$n_{H_2O}^0$ range with $n > 0$ (Fig. 6a). Figure 7 represents $\Delta V_E / \Delta V_G$ in the κ_{ch}–$n_{H_2O}^0$ space for various $n_{CO_2}^0$, which shows that abrupt changes in $\Delta V_E / \Delta V_G$ with κ_{ch} commonly occur for a wide range of $n_{CO_2}^0$. In summary, the magnitude of $\Delta V_E / \Delta V_G$ primarily depends on $n_{H_2O}^0$ and κ_{ch} and the dependencies are affected by $n_{CO_2}^0$, ρ_e and p to some extent.

The features of Fig. 6 and observed values of $\Delta V_E / \Delta V_G$ in Table 1 enable us to estimate the parameters related to the magma storage conditions during the 2011 and 2018 eruptions. In Fig. 7, we show the isopleths of the observed $\Delta V_E / \Delta V_G$ (2.69 and 2.33 for the 2011 and 2018 eruptions, respectively) in the color map of the calculated $\Delta V_E / \Delta V_G$ in the κ_{ch}–$n_{H_2O}^0$ space. In the lower-$n_{H_2O}^0$ range with no volatile exsolution ($n = 0$), the range of κ_{ch} for reproducing observed $\Delta V_E / \Delta V_G$ is ~ 4–5×10^{-11} Pa^{-1}. In the case of the higher-$n_{H_2O}^0$ range with volatile exsolution ($n > 0$), the range of κ_{ch} is substantially larger than that in the case of $n = 0$, and it depends on $n_{H_2O}^0$ and $n_{CO_2}^0$. In Fig. 7c, d, the values of $n_{CO_2}^0$ are set as 0.25 and 1.4 wt%, respectively, to cover the observed values from the chemical analysis of melt inclusion data (Saito et al. 2023). In this case, the volatile is always present

Kozono *et al. Earth, Planets and Space*   (2023) 75:100

Page 9 of 15
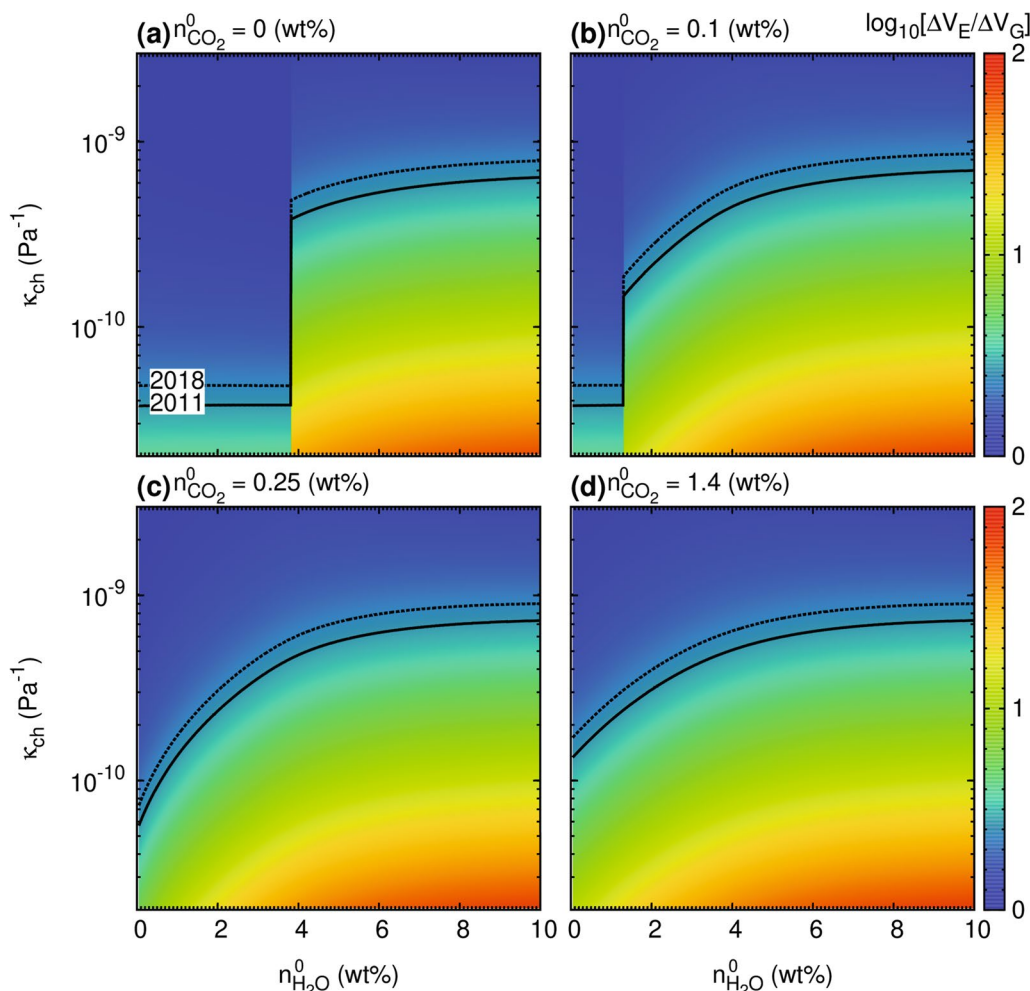
Fig. 7 $\Delta V_E / \Delta V_G$ in the space of κ_{ch} and $n^0_{H_2O}$ for $p = 245$ MPa and $\rho_e = 2500$ kg m^{-3} with varying $n^0_{CO_2}$, which was obtained from Eq. (7) or (9). Results for $n^0_{CO_2} = 0$ (**a**), 0.1 (**b**), 0.25 (**c**), and 1.4 wt% (**d**). Isopleths of the observed $\Delta V_E / \Delta V_G$ during the 2011 and 2018 eruptions (2.69 and 2.33, respectively) are also shown by solid and dashed curves, respectively

(i.e., $n > 0$) so that κ_{ch} which accounts for the observed values of $\Delta V_E / \Delta V_G$ increases with $n^0_{H_2O}$; the relationship between κ_{ch} and $n^0_{H_2O}$ (the $\kappa_{ch} - n^0_{H_2O}$ relationship) depends on $n^0_{CO_2}$ only in the case when $n^0_{H_2O}$ is close to 0 wt% (compare Fig. 7c, d). For all the cases from Fig. 7a–d, the feature of the $\kappa_{ch} - n^0_{H_2O}$ relationship is characterized by a strong increase in κ_{ch} with $n^0_{H_2O}$ when $n^0_{H_2O}$ is smaller than about 4 wt%. Figure 8 shows the dependence of the $\kappa_{ch} - n^0_{H_2O}$ relationship for $n^0_{CO_2} = 0.25$ wt% (cf. Figure 7c) on the erupted magma density (ρ_e) and the chamber pressure (p), where ρ_e and p are varied within realistic ranges (see Fig. 6b, c). Under these ranges, although the $\kappa_{ch} - n^0_{H_2O}$ relationship depends on both ρ_e and p in a quantitative sense, the main feature of the $\kappa_{ch} - n^0_{H_2O}$ relationship (i.e., the strong increase in κ_{ch} with $n^0_{H_2O}$ in the

range of $n^0_{H_2O} < 4$ wt%) does not change significantly (Fig. 8).

Figure 9 summarizes the possible ranges of κ_{ch} to achieve the observed $\Delta V_E / \Delta V_G$ during the 2011 and 2018 Shinmoe-dake eruptions (i.e., 2.69 and 2.33), where ρ_e and p are varied within realistic ranges. Under the observed range of $n^0_{CO_2}$ (0.25−1.4 wt%), where the condition of $n > 0$ is satisfied as shown in Fig. 7c, d, we considered three conditions for $n^0_{H_2O}$ as 2, 4, and 6.2 wt%. Here, the maximum value 6.2 wt% was estimated from melt inclusion data (Saito et al. 2023). In response to the feature of the $\kappa_{ch} - n^0_{H_2O}$ relationship, κ_{ch} increases with $n^0_{H_2O}$ and reaches $\sim 5 \times 10^{-10}-3.5 \times 10^{-9}$ Pa^{-1} for $n^0_{H_2O} = 6.2$ wt%. We also calculated the ranges of κ_{ch} using Eq. (9) under the assumption
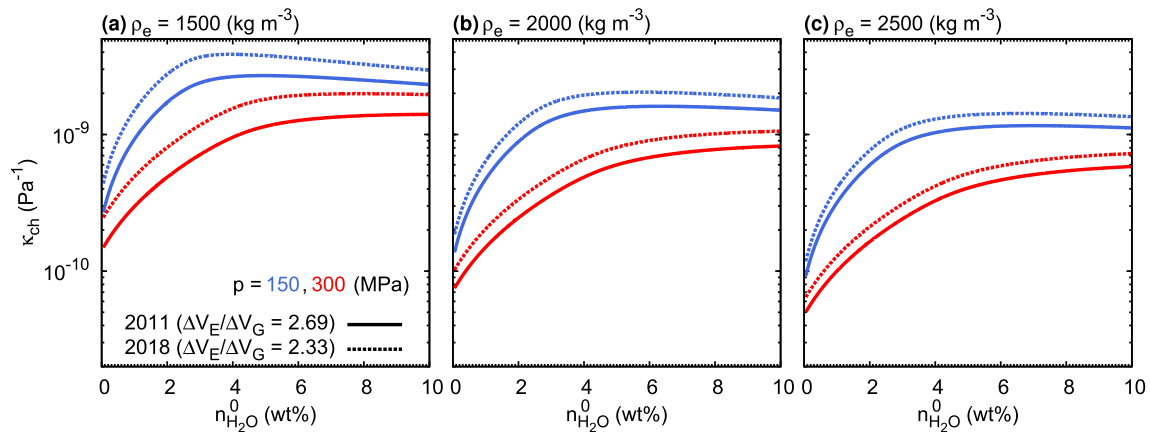
Fig. 8 Relationship between κ_{ch} and $n_{H_2O}^0$ for the observed values of $\Delta V_E/\Delta V_G$ during the 2011 (2.69; solid curves) and 2018 (2.33; dashed curves) eruptions, with varying p (150 and 300 MPa) and ρ_e (1500 (**a**), 2000 (**b**), and 2500 (**c**) kg m^{-3}. The results are obtained from Eq. (7), where $n_{CO_2}^0$ is set as 0.25 wt%

that $n = 0$, which corresponds to the condition of no gas phase in the magma such as due to lower volatile contents (e.g., Fig. 7a, b). In this case, κ_{ch} is limited to a smaller range (4×10^{-11}–1.5×10^{-10} Pa^{-1}) compared to the case of $n > 0$.

Discussion

By using the analytical expression for the volume ratio ($\Delta V_E/\Delta V_G$), we have specified the range of the effective chamber compressibility (κ_{ch}) to account for the observed values of $\Delta V_E/\Delta V_G$ during the 2011 and 2018 eruptions at Shinmoe-dake volcano. Here, κ_{ch} depends on the rigidity of the surrounding host rocks and chamber shape. To assess the effects of rigidity and various chamber shapes on κ_{ch}, we consider an ellipsoid embedded into an elastic half-space, in which one of the semiaxes (r_v) is vertical and the other two semiaxes (r_h) are horizontal and have the same magnitude. When r_v is equal to r_h, the chamber shape is purely spherical. In this case, κ_{ch} is expressed as $3/(4\mu)$, where μ is the rigidity of the surrounding host rocks. When $r_v \neq r_h$, the chamber sources correspond to oblate and prolate spheroids for $r_v < r_h$ and $r_v > r_h$, respectively. We numerically calculated the compressibility ratio of the ellipsoidal to spherical sources as a function of the aspect ratio of the vertical to horizontal semiaxes (r_v/r_h) based on a finite element method using COMSOL Multiphysics software (Fig. 10), and the calculated values were consistent with those of previous studies (Amoruso and Crescentini 2009; Anderson and Segall 2011). The compressibility ratio is greater than 1 for $r_v \neq r_h$, indicating that the effective compressibility of the ellipsoidal source is larger than that of the spherical source. When $r_v > r_h$, the compressibility ratio is limited to the range of 1–4/3 (Amoruso and Crescentini 2009).

In contrast, when $r_v < r_h$, the compressibility ratio drastically increases with decreasing r_v/r_h, and it reaches 10 for $r_v/r_h \sim 10^{-1}$. In Fig. 10, we also investigated the dependence of the compressibility ratio on the chamber depth (d) that is normalized to the radius of a sphere with an equivalent volume (r). For a given r_v/r_h, the compressibility ratio increases with decreasing (d/r), which is also consistent with a previous study (Anderson and Segall 2011).

The rigidity of the surrounding host rocks (μ) can be estimated from the seismic velocity structure beneath the volcano. For example, by using the P-wave velocity (v_p), μ is expressed as $\rho_{cr}v_p^2(1 - 2\nu)/(2 - 2\nu)$ where ρ_{cr} and ν are the crust density and the Poisson's ratio, respectively. The P-wave velocities beneath the Kirishima volcano group inferred from refraction analysis of the seismic experiment were 2.1, 3.6, and 5.8 km s^{-1} for three layers down to 3 km (below sea level) from the surface, where the thicknesses of the first (2.1 km s^{-1}) and second (3.6 km s^{-1}) layers around the center of the volcano group were ~ 0.5 and 2 km, respectively (Tsutsui et al. 1996). Under these velocity ranges and assuming that $\rho_{cr} \sim 2500$ kg m^{-3} and $\nu = 0.25$, μ is estimated to be 3.7–28 GPa.

Using the rigidity estimated from the seismic velocity and assessing the chamber shape effects described in Fig. 10, we can calculate the possible range of κ_{ch} (the right side of Fig. 9). In the case of the spherical chamber (i.e., $r_v/r_h = 1$), the possible range of κ_{ch} is estimated at $\sim 3 \times 10^{-11}$–2×10^{-10} Pa^{-1}. When $r_v/r_h = 0.1$, which corresponds to the oblate spheroid, the possible range of κ_{ch} is estimated at $\sim 1.5 \times 10^{-10}$–3×10^{-9} Pa^{-1}. A comparison between these possible ranges and κ_{ch} estimated from $\Delta V_E/\Delta V_G$ (Fig. 9)

Kozono *et al. Earth, Planets and Space*   (2023) 75:100

Page 11 of 15
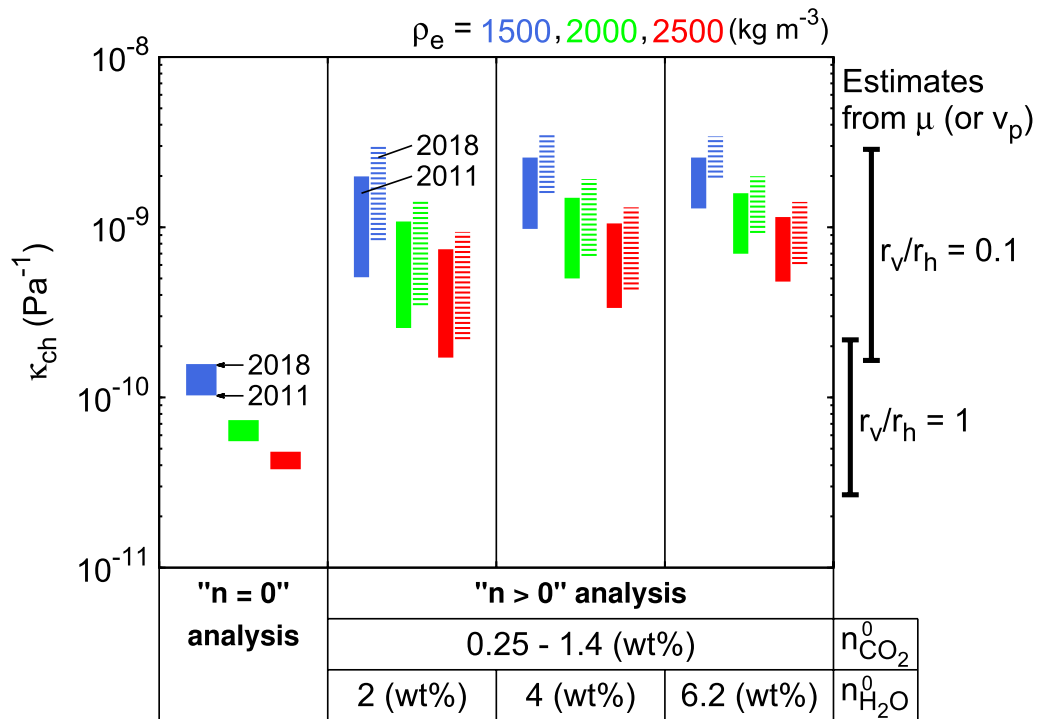
Fig. 9 Possible ranges of the effective chamber compressibility (κ_{ch}) for $\Delta V_E/\Delta V_G = 2.69$ and 2.33 (values of the 2011 and 2018 eruptions, respectively), $p = 150$–300 MPa, and $\rho_e = 1500$, 2000, and 2500 kg m^{-3} under the assumption that $n > 0$ or $n = 0$. In the analysis of $n > 0$ for $n^0_{CO_2} = 0.25$–1.4 wt%, we assumed three conditions for $n^0_{H_2O}$ (2, 4, and 6.2 wt%). The results for $\Delta V_E/\Delta V_G = 2.69$ (2011) and 2.33 (2018) are shown by solid and dashed bars, respectively. For the results with $n = 0$, the minimum and maximum ends of the bar correspond to κ_{ch} values of $\Delta V_E/\Delta V_G = 2.69$ (2011) and 2.33 (2018), respectively. On the right side of the figure, we show the range of κ_{ch} estimated from the rigidity of the surrounding host rocks (μ) calculated by using P-wave velocity (v_p) beneath Shinmoe-dake (Tsutsui et al. 1996) under types of the chamber shape ($r_v/r_h = 1$ for sphere and $r_v/r_h = 0.1$ for oblate spheroid; see Fig. 10). The value of d/r, defined in Fig. 10, varies from 1 to 10
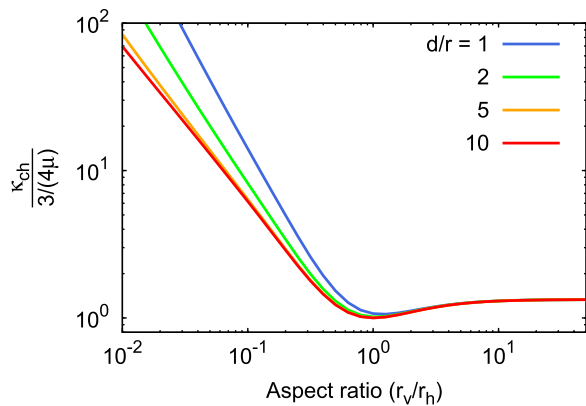
Fig. 10 Reproduction of Fig. 5 in Anderson and Segall (2011), showing the ratio of the effective magma chamber compressibility (κ_{ch}) of an ellipsoidal source in an elastic half-space to that of a spherical source in a full space ($3/(4\mu)$) as a function of aspect ratio between the semiaxes of the ellipsoid (r_v/r_h, where r_v and r_h are vertical and horizontal axes, respectively). The results were numerically obtained using the finite element method. The chamber volume is kept constant, and the ratio of the distance from the surface to the top of the chamber (d) to the radius of a sphere with an equivalent volume (r) is varied

indicates that the estimate of κ_{ch} for $n > 0$ is consistent with the possible range for $r_v/r_h = 0.1$, whereas the estimate of κ_{ch} for $n = 0$ is consistent with the possible range for the spherical chamber (i.e., $r_v/r_h = 1$). In the inversion process of the deformation source determination during the 2011 Shinmoe-dake eruption, various source models composed of a spherical or dike source, or multiple sources with two spherical or two dike sources, or a spherical + dike sources were tested, and AIC analyses suggest that the single spherical source model was the most likely among these source models (Ueda et al. 2013). This implies that the condition of $n = 0$ is required to reproduce κ_{ch} under the observed geodetic data and $\Delta V_E/\Delta V_G$ in 2011. In Eqs. (7) and (9), we define n_0 as the initial volatile content. This definition implicitly assumes a closed system in which the gas phase (i,e., bubbles) continues to exist within the chamber. When such a closed system is assumed, the melt inclusion data ($n^0_{CO_2} = 0.25$–1.4 wt% and $n^0_{H_2O} = 6.2$ wt%; Saito et al. 2023) leads to the condition of $n > 0$. However, if we consider a system where bubbles efficiently segregate from the magma (i.e.,

Kozono *et al. Earth, Planets and Space*   (2023) 75:100

Page 12 of 15

open system), the magma compressibility approaches the liquid-crystals compressibility (Eq. 8); as a result, $\Delta V_E/\Delta V_G$ can be as small as that for $n = 0$ (Eq. 9). Therefore, efficient gas segregation likely occurred prior to the 2011 eruption. Although the deformation source in 2018 has not been strongly constrained because of the lack of AIC information, the estimates of κ_{ch} for the 2018 eruption also suggest the condition of $n = 0$ if we assume a spherical source based on the similarity of the deformation pattern between 2011 and 2018 (Fig. 1).

Finally, we point out that further analyses of the geodetic data considering the various shape of the deformation source are necessary for future assessments. One of the methods of performing detailed assessments of storage conditions is a more sophisticated joint inversion of multi-observation data. In the present analysis based on Ueda et al. (2013), information about the deformation source, such as the position, shape, and volume change, was obtained only from the inversion of the geodetic data. However, our results based on Eqs. (7) and (9) indicate that the geodetic source information has a complex relationship with other geological and magmatic parameters, such as the erupted magma volume, volatile contents, and rigidity of surrounding host rocks. A joint inversion that combines all the parameters included in Eqs. (7) and (9) may provide strong constraints on the magma storage and plumbing system, in which appropriate parameter values are simultaneously estimated. To solve the inversion problem that consists of a large number of parameters and assess the uncertainty of the parameter estimation, sophisticated inversion techniques based on the Bayesian framework (e.g., Markov Chain Monte Carlo (MCMC) method) are necessary. This kind of approach has been successfully applied to the long-term and episodic activities of Kīlauea volcano (Anderson and Poland 2016; Anderson et al. 2019). Applying a similar approach to the Shinmoe-dake eruptions is a promising direction for future research.

Conclusions

We specified the magma storage conditions prior to the 2011 and 2018 eruptions of Shinmoe-dake volcano based on the relationship between the geodetic volume change of the magma chamber and the erupted magma volume. We showed the analytical expression for the ratio of the erupted volume to the geodetic volume change (the volume ratio), which was formulated as a function of the magma storage conditions. This expression indicated that the volume ratio was strongly dependent on the effective compressibility of the magma chamber. In the Shinmoe-dake eruptions, the deflation of the spherical magma chamber accompanied by the lava effusion was detected by the geodetic observations and the geodetic volume change of the deflation source was estimated. In addition, the volumes of the erupted lava in the two eruptions were also estimated based on day-by-day SAR image analyses of the lava accumulation inside the summit crater. Based on these observations, we calculated the volume ratio by setting a proper time window in which the lava effusion was confidentially observed. By substituting the observed volume ratio into the analytical expression, we estimated the possible range of the effective chamber compressibility during the Shinmoe-dake eruptions. The effective chamber compressibility was also estimated using the rigidity of the surrounding host rocks and by assessing the chamber shape effects, where the rigidity was calculated from the seismic velocity. A comparison between these estimates revealed that under the assumption that the magma chamber is spherical, bubble-free magma in the chamber originating from efficient gas segregation under an open system is needed to explain the observed geodetic data and volume ratio. Our results indicate that combining multi-observation data based on the volume ratio provides valuable information about the magma storage process, such as the behavior of the gas phase in the magma chamber. Further analysis based on more sophisticated inversions of the multi-observation data may promote a detailed understanding of the magma chamber dynamics.

Appendix

In this appendix, we show the complete forms of the density and compressibility of the liquid (ρ_l and κ_l) and crystals (ρ_c and κ_c) as well as n, R, dn/dp, and dR/dp used in Eqs. (7) and (9).

The dependence of the liquid density ρ_l on temperature, pressure, and melt composition is modeled based on Lange and Carmichael (1990) and Iacovino and Till (2019) as follows:

$$\rho_l = \frac{\sum^i [X_i M_i]}{V_l}, \tag{10}$$

where X_i and M_i are the mole fraction and molecular weight of oxide component i in the melt, and V_l is the volume of liquid:

Kozono *et al. Earth, Planets and Space*   (2023) 75:100

Page 13 of 15

$$V_l = \sum^i \left[\overline{V}_i(T_{ref}, p_a) + \frac{d\overline{V}_i}{dT}(T - T_{ref}) + \frac{d\overline{V}_i}{dp}(p - p_a) \right] X_i. \tag{11}$$

Here, $V_i(T_{ref}, p_a)$ is the partial molar volume of component i in the liquid at reference temperature T_{ref} and atmospheric pressure p_a ($= 10^5$ Pa) and $d\overline{V}_i/dT$ and $d\overline{V}_i/dp$ are the temperature and pressure derivatives of the partial molar volume of component i. The values of $V_i(T_{ref}, p_a)$, $d\overline{V}_i/dT$, and $d\overline{V}_i/dp$ are summarized in Lesher and Spera (2015), and the oxide components are SiO_2, TiO_2, Al_2O_3, FeO, MgO, CaO, Na_2O, K_2O, H_2O, and CO_2. Using Eq. (10), the liquid compressibility κ_l is obtained as follows:

$$\kappa_l \equiv \frac{1}{\rho_l}\frac{d\rho_l}{dp} = -\frac{1}{V_l}\sum^i \frac{d\overline{V}_i}{dp}X_i. \tag{12}$$

The density and the compressibility of the crystals (ρ_c and κ_c) are expressed as follows:

$$\rho_c = \frac{\sum^j [\beta_j \rho_{cj}]}{\beta}, \tag{13}$$

and

$$\kappa_c \equiv \frac{1}{\rho_c}\frac{d\rho_c}{dp} = \frac{\sum^j [\beta_j \rho_{cj}\kappa_{cj}]}{\beta\rho_c}, \tag{14}$$

where the subscript j corresponds to crystal species and κ_{cj} is the compressibility of crystal j, which can be calculated from the inverse of the bulk modulus of the crystal. The crystals of the basaltic andesite magma in the deep magma chamber are reported to be olivine (3.4 vol.%) and high-An plagioclase (5.5 vol.%) (Suzuki et al. 2013). The bulk moduli of olivine and high-An plagioclase were set as 120 and 80 GPa, respectively (Mao et al. 2015; Brown et al. 2016).

The gas constant R for the H_2O–CO_2 mixture is expressed as follows:

$$R = \left(\frac{n^0_{H_2O} - n_l c_{H_2O}}{M_{H_2O}} + \frac{n^0_{CO_2} - n_l c_{CO_2}}{M_{CO_2}} \right) \frac{R'}{1 - n_l c}, \tag{15}$$

where M_{H_2O} and M_{CO_2} are the molecular weights of H_2O and CO_2, respectively, and R' is the molar gas constant (8.314 J K^{-1} mol^{-1}). The pressure derivatives of R and n, which are used in Eq. (7), are obtained from Eqs. (5) and (15) as follows:

$$\frac{dR}{dp} = \left[\frac{(c_{CO_2} n^0_{H_2O} - c_{H_2O} n^0_{CO_2})\beta\rho_c(\kappa_l - \kappa_c)}{\rho_{lc}} \right.$$
$$- \frac{dc_{H_2O}}{dp}(n^0_{CO_2} - n_l c_{CO_2}) + \frac{dc_{CO_2}}{dp}(n^0_{H_2O} - n_l c_{H_2O}) \bigg]$$
$$\times \frac{(M_{CO_2} - M_{H_2O})n_l R'}{M_{H_2O}M_{CO_2}(n_0 - n_l c)^2}, \tag{16}$$

and

$$\frac{dn}{dp} = -\left[\frac{c\beta\rho_c(\kappa_l - \kappa_c)}{\rho_{lc}} + \frac{dc}{dp} \right] \frac{n_l(1 - n_0)}{(1 - n_l c)^2}, \tag{17}$$

respectively.

The dissolved H_2O and CO_2 concentrations (c_{H_2O} and c_{CO_2}) and total concentration c ($= c_{H_2O} + c_{CO_2}$) are calculated based on the solubility model by Iacono-Marziano et al. (2012), which enables us to express the concentration as a function of mole fraction of H_2O in the gas phase (x_{H_2O}) for given temperature, pressure, and melt composition. The pressure derivatives of the concentration (dc_{H_2O}/dp, dc_{CO_2}/dp and dc/dp) are numerically calculated.

The above formulation enables us to describe $\Delta V_E / \Delta V_G$ as a function of x_{H_2O} for specific pressures and magmatic properties. In the numerical procedure, we first determine x_{H_2O} using the following relation:

$$\frac{x_{CO_2}}{x_{H_2O}} = \frac{1 - x_{H_2O}}{x_{H_2O}} = \frac{(n^0_{CO_2} - n_l c_{CO_2})M_{H_2O}}{(n^0_{H_2O} - n_l c_{H_2O})M_{CO_2}}, \tag{18}$$

where x_{CO_2} is the mole fraction of CO_2 in the gas phase. Equation (18) is used for implicitly determining x_{H_2O}.

Kozono *et al. Earth, Planets and Space*   (2023) 75:100

Page 14 of 15

Declarations

Competing interests
The authors declare that they have no competing interests.

Author details
[1]National Research Institute for Earth Science and Disaster Resilience, 3-1, Tennodai, Tsukuba, Ibaraki 305-0006, Japan. [2]Earthquake Research Institute, University of Tokyo, 1-1-1 Yayoi, Bunkyo-ku, Tokyo 113-0032, Japan. [3]Geological Survey of Japan, AIST, 1-1-1, Higashi, Tsukuba, Ibaraki 305-8567, Japan.

References
Aizawa K, Koyama T, Hase H, Uyeshima M, Kanda W, Utsugi M, Yoshimura R, Yamaya Y, Hashimoto T, Yamazaki K, Komatsu S, Watanabe A, Miyakawa K, Ogawa Y (2014) Three-dimensional resistivity structure and magma plumbing system of the Kirishima Volcanoes as inferred from broadband magnetotelluric data. J Geophys Res 119(1):198–215. https://doi.org/10.1002/2013JB010682

Amoruso A, Crescentini L (2009) Shape and volume change of pressurized ellipsoidal cavities from deformation and seismic data. J Geophys Res 114(B2):B02210. https://doi.org/10.1029/2008JB005946

Anderson KR, Johanson IA, Patrick MR, Gu M, Segall P, Poland MP, Montgomery-Brown EK, Miklius A (2019) Magma reservoir failure and the onset of caldera collapse at Kīlauea Volcano in 2018. Science. https://doi.org/10.1126/science.aaz1822s

Anderson KR, Poland MP (2016) Bayesian estimation of magma supply, storage, and eruption rates using a multiphysical volcano model: Kīlauea Volcano, 2000-2012. Earth Planet Sci Lett 447:161–171. https://doi.org/10.1016/j.epsl.2016.04.029

Anderson K, Segall P (2011) Physics-based models of ground deformation and extrusion rate at effusively erupting volcanoes. J Geophys Res 116:B07204. https://doi.org/10.1029/2010JB007939

Brown JM, Angel RJ, Ross NL (2016) Elasticity of plagioclase feldspars. J Geophys Res 121(2):663–675. https://doi.org/10.1002/2015JB012736

Devine JD, Murphy MD, Rutherford MJ, Barclay J, Sparks RSJ, Carroll MR, Young SR, Gardner JE (1998) Petrologic evidence for pre-eruptive pressure-temperature conditions, and recent reheating, of andesitic magma erupting at the Soufriere Hills Volcano. Montserrat, W.I. Geophys Res Lett 25(19):3669–3672. https://doi.org/10.1029/98GL01330

Dvorak JJ, Dzurisin D (1997) Volcano geodesy: The search for magma reservoirs and the formation of eruptive vents. Rev Geophys 35(3):343–384. https://doi.org/10.1029/97RG00070

Dzurisin D (2003) A comprehensive approach to monitoring volcano deformation as a window on the eruption cycle. Rev Geophys. https://doi.org/10.1029/2001RG000107

Hill GJ, Caldwell TG, Heise W, Chertkoff DG, Bibby HM, Burgess MK, Cull JP, Cas RAF (2009) Distribution of melt beneath Mount St Helens and Mount Adams inferred from magnetotelluric data. Nature Geosci 2(11):785–789. https://doi.org/10.1038/ngeo661

Hreinsdóttir S, Sigmundsson F, Roberts MJ, Björnsson H, R G, Arason P, Árnadóttir T, Hólmjárn J, Geirsson H, Bennett RA, Gudmundsson MT, Oddsson B, Ofeigsson BG, Villemin T, Jonsson T, Sturkell E, Hoskuldsson A, Larsen G, Thordarson T, (2014) Volcanic plume height correlated with magma-pressure change at Grimsvotn Volcano, iceland. Nature Geosci 7(3):214–218. https://doi.org/10.1038/ngeo2044

Huppert H, Woods AW (2002) The role of volatiles in magma chamber dynamics. Nature 420(6915):493–495. https://doi.org/10.1038/nature01211

Iacono-Marziano G, Morizet Y, Le Trong E, Gaillard F (2012) New experimental data and semi-empirical parameterization of H_2O-CO_2 solubility in mafic melts. Geochim Cosmochim Acta 97:1–23. https://doi.org/10.1016/j.gca.2012.08.035

Iacovino K, Till CB (2019) DensityX: A program for calculating the densities of magmatic liquids up to 1,627°C and 30 kbar. Volcanica 2(1):1–10. https://doi.org/10.30909/vol.02.01.0110

Kozono T (2021) The dynamics of dual-magma-chamber system during volcanic eruptions inferred from physical modeling. Earth Planets Space 73(1):1–11. https://doi.org/10.1186/s40623-021-01421-4

Kozono T, Koyaguchi T (2009) Effects of relative motion between gas and liquid on 1-dimensional steady flow in silicic volcanic conduits: 1. An analytical method. J Volcanol Geotherm Res 180(1):21–36. https://doi.org/10.1016/j.jvolgeores.2008.11.006

Kozono T, Ueda H, Ozawa T, Koyaguchi T, Fujita E, Tomiya A, Suzuki YJ (2013) Magma discharge variations during the 2011 eruptions of Shinmoe-dake volcano, Japan, revealed by geodetic and satellite observations. Bull Volcanol 75(3):695. https://doi.org/10.1007/s00445-013-0695-4

Kozono T, Ueda H, Shimbori T, Fukui K (2014) Correlation between magma chamber deflation and eruption cloud height during the 2011 Shinmoe-dake eruptions. Earth Planets Space 66(1):139. https://doi.org/10.1186/s40623-014-0139-1

Lange R, Carmichael IS (1990) Thermodynamic properties of silicate liquids with emphasis on density, thermal expansion and compressibility. Rev Mineral Geochem 24(1):25–64

Lees JM (2007) Seismic tomography of magmatic systems. J Volcanol Geotherm Res 167(1):37–56. https://doi.org/10.1016/j.jvolgeores.2007.06.008

Lesher CE, Spera FJ (2015) Thermodynamic and transport properties of silicate melts and magma. In: The Encyclopedia of Volcanoes. Elsevier, pp 113–141

Mao Z, Fan D, Lin JF, Yang J, Tkachev SN, Zhuravlev K, Prakapenka VB (2015) Elasticity of single-crystal olivine at high pressures and temperatures. Earth Planet Sci Lett 426:204–215. https://doi.org/10.1016/j.epsl.2015.06.045

Mastin LG, Roeloffs E, Beeler NM, Quick JE (2008) Constraints on the size, overpressure, and volatile content of the Mount St. Helens magma system from geodetic and dome-growth measurements during the 2004–2006+ eruption. US Geol Surv Prof Pap 1750:461–492. https://doi.org/10.3133/pp175022

Nakada S, Nagai M, Kaneko T, Suzuki Y, Maeno F (2013) The outline of the 2011 eruption at Shinmoe-dake (Kirishima), Japan. Earth Planets Space 65(6):475–488. https://doi.org/10.5047/eps.2013.03.016

Nakao S, Morita Y, Yakiwara H, Oikawa J, Ueda H, Takahashi H, Ohta Y, Matsushima T, Iguchi M (2013) Volume change of the magma reservoir relating to the 2011 Kirishima Shinmoe-dake eruption: Charging, discharging and recharging process inferred from GPS measurements. Earth Planets Space 65(6):3. https://doi.org/10.5047/eps.2013.05.017

NIED (2018) Temporal variation of the Shinmoe-dake crater in the 2018 eruption revealed by spaceborne SAR observations. Representative Coordinator Community for Prediction of Volcanic Eruptions 141:159–164 **(in Japanese)**

Ozawa T, Kozono T (2013) Temporal variation of the Shinmoe-dake crater in the 2011 eruption revealed by spaceborne SAR observations. Earth Planets Space 65(6):527–537. https://doi.org/10.5047/eps.2013.05.004

Rivalta E, Segall P (2008) Magma compressibility and the missing source for some dike intrusions. Geophys Res Lett. https://doi.org/10.1029/2007GL032521

Rubin AM (1995) Propagation of magma-filled cracks. Annu Rev Earth Planet Sci 23(1):287–336. https://doi.org/10.1146/annurev.ea.23.050195.001443

Saito G, Oikawa T, Ishizuka O (2023) Magma ascent and degassing processes of the 2011 and 2017–18 eruptions of Shinmoedake in Kirishima volcano group, Japan, based on petrological characteristics and volatile content of magmas. Earth Planets Space 75:89. https://doi.org/10.1186/s40623-023-01836-1

Segall P (2010) Earthquake and volcano deformation. Princeton University Press, Princeton

Shimbori T, Sakurai T, Tahara M, Fukui K (2013) Observation of eruption clouds with weather radars and meteorological satellites: a case study of the eruptions at Shinmoedake volcano in 2011. Q J Seismol 77:139–325 **(in Japanese with English abstract)**

Slezin YB (2003) The mechanism of volcanic eruptions (a steady state approach). J Volcanol Geotherm Res 122(1–2):7–50. https://doi.org/10.1016/S0377-0273(02)00464-X

Suzuki Y, Yasuda A, Hokanishi N, Kaneko T, Nakada S, Fujii T (2013) Syneruptive deep magma transfer and shallow magma remobilization during the 2011 eruption of Shinmoe-dake, Japan-Constraints from melt inclusions and phase equilibria experiments. J Volcanol Geotherm Res 257:184–204. https://doi.org/10.1016/j.jvolgeores.2013.03.017

Tait S, Jaupart C, Vergniolle S (1989) Pressure, gas content and eruption perio-
dicity of a shallow, crystallising magma chamber. Earth Planet Sci Lett
92(1):107–123. https://doi.org/10.1016/0012-821X(89)90025-3

Tomiya A, Miyagi I, Saito G, Geshi N (2013) Short time scales of magma-mixing
processes prior to the 2011 eruption of Shinmoedake volcano, Kirishima
volcanic group, Japan. Bull Volcanol 75(10):750. https://doi.org/10.1007/
s00445-013-0750-1

Tsutsui T, Kagiyama T, Mikada H, Morita Y, Matsushima T, Iguchi M et al (1996)
Seismic velocity structure beneath Kirishima volcanoes with differential
analysis of explosion experiment. Bull Volcanol Soc Japan 41(6):227–241.
(in Japanese with English abstract) https://doi.org/10.18940/kazan.
41.5_227

Ueda H (2018) Mechanism of the Shinmoe-dake eruptions in 2011 and 2018
inferred from crustal deformation data. Abstract 2018 Fall Meeting of the
Volcanological Society of Japan A1-11:p12 **(in Japanese)**

Ueda H, Kozono T, Fujita E, Kohno Y, Nagai M, Miyagi Y, Tanada T (2013)
Crustal deformation associated with the 2011 Shinmoe-dake eruption
as observed by tiltmeters and GPS. Earth Planets Space 65(6):517–525.
https://doi.org/10.5047/eps.2013.03.001

Waite GP, Moran SC (2009) VP structure of Mount St. Helens, Washington, USA,
imaged with local earthquake tomography. J Volcanol Geotherm Res
182(1):113–122. https://doi.org/10.1016/j.jvolgeores.2009.02.009

Wessel P, Smith WHF, Scharroo R, Luis J, Wobbe F (2013) Generic mapping
tools: improved version released. Eos Trans AGU 94(45):409–410. https://
doi.org/10.1002/2013EO450001

Woods AW, Huppert HE (2003) On magma chamber evolution during slow
effusive eruptions. J Geophys Res. https://doi.org/10.1029/2002JB002019

Woods AW, Koyaguchi T (1994) Transitions between explosive and effusive
eruptions of silicic magmas. Nature 370:641–644. https://doi.org/10.1038/
370641a0

Yamada T, Ueda H, Mori T, Tanada T (2019) Tracing volcanic activity chronol-
ogy from a multiparameter dataset at Shinmoedake volcano (Kirishima),
Japan. J Disast Res 14(5):687–700. https://doi.org/10.20965/jdr.2019.
p0687

Publisher's Note